# Excitonic Emissions and Above-Bandgap Luminescence in Single Crystal Perovskite Semiconductors $CsPbBr_3$ and $CsPbCl_3$

M. Sebastian[1], J.A. Peters[1], C. C. Stoumpos[2], J. Im[3], S. S. Kostina[1], Z. Liu[1], M.G. Kanatzidis[2], A. J. Freeman[3], and B. W. Wessels[1]

*1 Dept. of Materials Science, Northwestern University, Evanston, IL 60208*

*2 Dept. of Chemistry, Northwestern University, Evanston, IL 60208*

*3 Dept. of Physics and Astronomy, Northwestern University, Evanston, IL 60208*

## Abstract

The ternary compounds $CsPbX_3$ (X= Br or Cl) have perovskite structures that are being considered for optical and electronic applications such as lasing and gamma ray detection. Above bandgap excitonic photoluminescence (PL) band is seen in both $CsPbX_3$ compounds. An exciton emission peak centered at 2.98 eV, ~0.1 eV above the room temperature bandgap, is observed for $CsPbCl_3$. The thermal quenching of the exciton luminescence intensity is well described by a two-step quenching model, yielding activation energies of 0.057 eV and 0.0076 eV for high and low temperature regimes, respectively. $CsPbBr_3$ exhibits excitonic luminescence peaks located at 2.29 eV and 2.33 eV that are attributed to recombination involving Br vacancy centers. Activation energies for thermal quenching of the excitonic luminescence of 0.017 eV and 0.0007 eV were calculated for $CsPbBr_3$. Temperature dependent PL experiments reveal unexpected blueshifts for all excitonic emission peaks in $CsPbX_3$ compounds. A phonon assisted step-up process leads to the blueshift in $CsPbBr_3$ emission, while there is a contribution from bandgap widening in $CsPbCl_3$. The absence of deep level defect luminescence within the bandgap in these compounds makes them attractive candidates for high resolution, room temperature radiation detection.

Keywords: photoluminescence (PL), exciton emission, gamma-ray detection, perovskite halides, $CsPbBr_3$, $CsPbCl_3$

## I. Introduction

The last few years have witnessed a dramatic increase of research on the halide perovskite compounds of group IV metal ions. This long-known class of semiconductors has been studied starting as far back as 1950's, mainly through the pioneering work of Moller on the $CsPbX_3$ compound (X = Cl, Br, I)[1-3]. Since then, these perovskite compounds have attracted much attention due to their remarkable optical[4,5,6] and electronic[7] properties and the numerous temperature-induced structural phase transitions[8,9,10]. The discovery that ignited the recent explosive growth in the field was the realization of efficient Dye-Sensitized Solar Cells (DSSC's) using $CH_3NH_3PbI_3$ as the light-absorbing component, thus achieving a 4% conversion efficiency[11]. After the initial discovery, the liquid electrolyte was eliminated in favor of an all-solid state photovoltaic device, marked by the successful employment of $CsSnI_3$[12] and $CH_3NH_3PbI_3$-based perovskites[13] as hole transport and light-absorber components, respectively. Currently, the perovskite solar cells are able to deliver conversion efficiencies of ~20%[14], clearly demonstrating the excellent photoconducting properties of the halide perovskite semiconductors. However, aside from the initial reports on photoconductivity of the $CsPbX_3$ compounds [1] only few experiments dealt with the charge-transport properties of these compounds and in most of them the measured electrical properties were attributed to ionic motion[15]. We recently focused our attention in the development of $CsPbX_3$[16,17] and other halide semiconductor compounds[18] to utilize their photo-conversion potential in the

field of high energy radiation detection.

Gamma ray spectroscopy is widely used in fields such as security, medicine, and astrophysics. For many of these applications, it is important to have materials that are able to detect gamma rays with high resolution at room temperature. This can be achieved by using semiconductors that have a large bandgap, high density, and optimal charge transport properties as given by the mobility-lifetime ($\mu\tau$) product. Current detector materials are semi-insulating semiconductors containing heavy elements, such as $Cd_{0.9}Zn_{0.1}Te$ (CZT) and TlBr [19]. These semiconductors have high resistivities (>$10^9$ Ω-cm) that result in low detector background noise, leading to high resolution gamma ray spectra. In addition the semiconductor CZT has a $\mu\tau$ value on the order of $10^{-2}$ $cm^2 \cdot V^{-1}$ and TlBr on the order of $10^{-3}$ $cm^2 \cdot V^{-1}$. There are, however, several drawbacks associated with these two compounds. CZT is known to exhibit twinning and Te precipitation formation that lowers the $\mu\tau$ value, whereas TlBr is mechanically soft and thus deleterious line defects are readily formed. In addition, TlBr suffers from electric polarization over time [19,20]. This results in a built-in field that impedes current flow in the material, causing a decrease in detector performance over time. These effects limit the detector efficiency and its spectral resolution.

As a result, other compounds such as the ternary compounds $CsPbX_3$ (X = Br, Cl) are being developed as room temperature x-ray and gamma ray detector materials due to their high density, high resistivity, $\mu\tau$ and wide bandgap [16,17]. Large single crystals of these

compounds were grown via modified Bridgman technique. Using laser illumination they were found to have direct bandgaps and high μτ values on the order of $10^{-3}$ $cm^2 \cdot V^{-1}$ for both electrons and holes stemming from the favorable electronic structure of the perovskite structure-type. In addition, $CsPbBr_3$ has already been shown to detect Ag X-rays [16,17]. Since these compounds are being considered as hard radiation detector materials, a number of relevant properties such as defect stability need to be understood. Even very low concentrations of native defects and impurities can serve as traps and recombination centers that degrade the detector performance [19]. Trapping of photo-excited carriers at defects decreases spectral resolution. Furthermore, surface recombination of carriers decreases the charge collection efficiency. The μτ value of a material is degraded by defect concentrations as low as a few ppm or even lower. Most chemically specific measurement techniques do not have the requisite sensitivity to detect defects at these low levels. In addition, they cannot detect native defects such as vacancies and anti-site defects which also result in decreased μτ values and detector efficiency. However, since many of these point defects are luminescent they can be detected by photoluminescence (PL) spectroscopy. Substitutional chemical impurities or native defects such as vacancies can manifest themselves as peaks in a PL spectrum, even at concentrations in the parts per billion range.

The crystal structures of $CsPbBr_3$ and $CsPbCl_3$ crystallize in the *Pnma* (or the equivalent *Pbnm*)[21] and *P*4*mm*[2] space groups, respectively, at room temperature (Fig. 1). These space

groups correspond to distorted perovskites structures, deviating from the ideal cubic structure (*Pm*-3*m* space group) as a result of tilting between adjacent $[PbX_6]^{4-}$octahedra. At elevated temperatures, the octahedral tilting is gradually lifted up to a phase transition temperature ($T_c$), above which the compounds form cubic perovskite structure. The $T_c$ lies at 48°C for $CsPbCl_3$. Meanwhile, $CsPbBr_3$ undergoes two successive transitions from orthorhombic to tetragonal and then to cubic with the respective transitions occurring at $T_c$'s of 80°C and 120°C. Both these compounds crystallize from the melt in the cubic form which enables uniform crystal growth. Unlike most structural transitions, the perovskite tree of transitions [22] includes mostly continuous phase changes which are fully reversible upon transformation and do not appear to result in any macroscopic damage to the as-grown crystal. Instead, the phase transitions only generate twin domains introducing some dislocations at the domain boundaries. Potentially, such dislocations are the origin of the unusual behavior of the halide atoms which adopt an anharmonic thermal behavior [10].

In the context of the discussion below, we have confirmed the room temperature structure of $CsPbBr_3$ in our previous work and we could also confirm that of $CsPbCl_3$ by refining the structure of the Bridgman-grown crystals. However, during cell indexing we have noticed the clear presence of supercell reflections in both compounds which can be indexed and refined as $\sqrt{2} \times \sqrt{2} \times 1$ and $2 \times 2 \times 2$ supercells for $CsPbBr_3$ and $CsPbCl_3$, respectively (Tables 1 and 2). Even though the final supercells have approximately the same volume, the qualitative characteristics

of the two lattices are different (Figure 1). The most striking difference between the two compounds comes from the atom that induces the structural ordering. In order to better highlight this difference, the atomic coordinates for both the subcells and the supercells are listed in Tables 3 and 4. By initially ignoring the symmetry breaking, both subcells contain four independent atoms with the halides occupying two crystallographic positions, on and about the 4-fold ($CsPbCl_3$) and pseudo 4-fold axis ($CsPbBr_3$). Upon ordering, it is only the $Cs^+$ ion of $CsPbCl_3$ that splits into 3 unique atoms while Pb and Cl are not affected by the ordering. In contrast, $CsPbBr_3$ undergoes a much less regio-selective ordering with all atomic positions splitting into four equivalent ones. Detailed crystallographic data are given in the Supporting Information. Crystallographic data for the $CsPbBr_3$ subcell are given elsewhere.[10b]

There are several prior PL studies of single crystal $CsPbX_3$ compounds [4,6,16,17,23-25]. PL measurements on single crystal samples of $CsPbBr_3$ have shown the presence of emission bands at 2.32 eV at temperatures up to 110 K that have been attributed to recombination of free excitons [4,6,16,17,23]. At 4.2 K, this peak is accompanied by several phonon replicas [4,23]. If this emission is indeed due to the free exciton it suggests that the compounds are nominally chemically pure and stoichiometric. However, a subsequent study of PL of single crystals of $CsPbBr_3$ grown by Bridgman revealed the presence of a broad peak below the band edge at 2.16 eV from 6 K up to 90 K [6]. This was attributed to emission from a defect or series of defect states, whose nature was not further investigated [6]. Previous PL measurements on

single crystal $CsPbCl_3$ indicated the presence of a free exciton peak at 2.98 eV, with additional peaks reported at 2.97, 2.96, and 2.94 eV [4]. The peak at 2.97 eV was tentatively attributed to either a bound exciton or edge luminescence, the peak at 2.96 eV to a phonon replica of the free exciton peak, and the peak at 2.94 eV was defect-related, possibly a bound exciton.

To determine the nature and origin of defects present in $CsPbX_3$ crystals grown by the Bridgman method, we have carried out both temperature and power dependent PL spectroscopy. Thermal quenching measurements enable determination of the activation energies of the luminescent defects [26,27]. Power dependent PL measurements are used to determine the defect species involved in radiative recombination: exciton, donor-acceptor pair (DAP), or free-to-bound excitonic transitions [26,28].

Here we report on temperature and power dependent PL measurements of undoped $CsPbX_3$ single crystals. For $CsPbBr_3$, luminescence emission is observed at 2.33 eV and 2.29 eV at 10 K, persisting up to room temperature. For $CsPbCl_3$, an exciton peak is observed at 2.98 eV, along with additional peaks at 2.94, 2.96, and 2.97eV. In both cases the luminescence emission is above the conduction band edge and is tentatively attributed to recombination involving halogen vacancy defect centers. Neither shallow nor deep level radiative defects are observed within the gap in these $CsPbX_3$ compounds.

## II. Experiment

Single crystal ingots of the compounds were grown by the vertical Bridgman method

143 using a four zone furnace with the temperature in the two top zones set to 700$^0$C and the two
144 lower zones operating at 300$^0$C. The crystals were pulled at a speed of 5.0 mm·h$^{-1}$ for $CsPbCl_3$
145 and 2.5 mm·h$^{-1}$ for $CsPbBr_3$, respectively. Wafers from the resulting single crystal ingot were cut
146 perpendicular to the growth direction and then polished using 4000 grit BN paper with WD-40
147 lubricant. The wafers were then rinsed with acetone and subsequently immersed in
148 concentrated aqueous HBr to remove surface damage. As a final step the samples were rinsed
149 with toluene. Further details of $CsPbX_3$ synthesis, growth, and processing are presented
150 elsewhere [17]. Small crystals that were suitable for X-ray diffraction were readily obtained
151 from the boule and mounted on a STOE II image plate single-crystal diffractometer. The crystal
152 structures of the compounds were solved and refined using the SHELXL-2013 suite[29], aided
153 by special functions of the PLATON[30] and WINGX[31] program suites. The as-grown crystal is
154 semi-insulating with a resistivity ~$10^{10}$ Ω-cm [17].

155 For PL measurements, the 405 nm line from a CW semiconductor diode laser is the
156 excitation source. For temperature-dependent PL measurements, the excitation intensity was
157 kept constant at 31.6 mW for $CsPbBr_3$ and at 15.8 mW for $CsPbCl_3$ as this was found to give the
158 maximum overall PL intensity at 10K. For the power-dependent PL measurement, the same
159 excitation source was used, with a series of neutral optical density filters employed to vary the
160 incident laser power from 2.0 to up to 50 mW for $CsPbCl_3$ and from 2.0 to up to 91 mW for
161 $CsPbBr_3$. An optical chopper and lock-in amplifier were used to improve signal to noise ratio.

The PL emission spectra were resolved through the 0.75 m SPEX grating monochromator and detected by a Hamamatsu photomultiplier tube (R928). The sample was cooled to 10 K using a closed-cycle He cryostat (SHI cryogenics DE-202).

First-principles calculations were performed in order to determine thermodynamic properties of intrinsic defects for the case of $CsPbBr_3$. The projector augmented wave method[32] was implemented in the VASP code [33]. The generalized gradient approximation (GGA) method within the Perdew-Burke-Ernzerhof formalism [34] was employed for the exchange correlation functional, and the Heyd-Scuseria-Ernzerhof hybrid functional[35] was used to correct the band gap underestimation of the semi-local functional. The formation energy of defect *D* in charge state $q(\Delta H_{D,q})$was calculated with the following formula,

$$\Delta H_{D,q} = E(D^q) - E(Bulk) - \sum_i n_i \mu_i + qE_F + E_{corr}, \qquad 1$$

where *E* is the total energy of a bulk or a defect system in a charge state $q$, $n_i$ is a number of the atom $i$ which is removed (n<0) or added (n>0) to form defect $D$, $\mu_i$ is the corresponding chemical potential of the element $i$, and $E_F$ is the Fermi level [36]. Chemical potential $\mu_i$ is determined with a growth condition and Fermi level $E_F$ is determined self-consistently within the charge neutrality condition under the given growth temperature ($T_g$). $E_{corr}$ is a correction term including the finite cell correction [37] and band gap correction [38]. The defect level was determined with the charge transition level from q to q' $\varepsilon(q/q')$defined by

$$\varepsilon(q/q') = \left(\Delta H_D(D,q) - \Delta H_D(D,q')\right)/(q' - q) \qquad 2$$

To describe isolated defect configurations, a 2x2x2 supercell which accommodates 160 atoms was used. A 3x3x3 k-point mesh was used for momentum space integration.

## III. Results and discussion

*Temperature-dependent PL studies*

The PL spectra of $CsPbBr_3$ from 10 K to 180 K are shown in Fig. 2a. Scans from 1.5 to 3.0 eV show a single narrow emission peak centered at 2.32 eV. The inset of Fig. 2a shows the decomposition of the spectrum at 10 K, where 2 peaks (at 2.33 eV and 2.29 eV) are observed using a Gaussian decomposition. The peak centered at 2.33 eV has been previously assigned to a free exciton peak emission [4,6,23], while the peak located at 2.29 eV has been previously attributed to either a phonon replica of the free exciton [4] or to recombination involving a bound exciton state[6]. The room temperature bandgap for $CsPbBr_3$ crystal is ~2.23 eV (Fig. 3a). The absorption edge does not match the energy of the room temperature PL emission and therefore the excitonic emission in these compounds is not due to band-to-band recombination as previously reported. This suggests that the luminescence involves a center with a level in the conduction band.

The origin of the above bandgap luminescence in $CsPbBr_3$ was investigated using DFT calculations to determine defect stability. States ~0.23 eV and ~0.24 eV above the conduction band edge due to Br vacancies are predicted. This indicates that a recombination pathway via bound excitons exists that would result in PL peak with energies of ~2.46 eV and ~2.47 eV,

respectively. These calculations are in reasonable agreement with earlier DFT calculations on this compound by Shi and Du[39] which indicated a Br vacancy located at 0.16 eV above the conduction band minimum. The observed room temperature PL peak located at ~2.38 eV (~0.16 eV above the bandgap) is tentatively attributed to bound exciton recombination involving a Br vacancy defect, in excellent agreement with theory. Recently, such above bandgap PL emission at room temperature in organo-lead halide perovskite $CH_3NH_3PbI_3$ was observed but attributed to free carrier generation through rapid exciton dissociation [40].

PL studies of $CsPbCl_3$ in the 1.5 to 3.0 eV range reveal a narrow peak overlapped on a broad shoulder centered at ~2.97 eV (Fig. 2b). Gaussian decomposition of these PL signals (Fig. 2b inset) below 100 K reveals four peaks centered at 2.94, 2.96, 2.97, and 2.98 eV. Above 100K and up to 290 K, only the latter three peaks listed are observed. The room temperature bandgap for $CsPbCl_3$ crystal is 2.85 eV (Fig. 3b), thus all the PL emission peaks in Fig. 2b are above the bandgap. The peak centered at 2.98 eV could presumably be attributed to an exciton bound to a higher-lying state within the conduction band such as in the case for $CsPbBr_3$; with phonon replicas centered at 2.96 eV and 2.94 eV. A peak at 2.97 eV in $CsPbCl_3$ was previously attributed to a bound exciton [4] which is likely the identity of the 2.97 eV peak in this study.

All emission peaks of $CsPbBr_3$ and $CsPbCl_3$ blueshift with increasing temperature (Figs. 4a and 4b, respectively). This is unexpected since exciton PL typically redshifts with temperature due to bandgap shrinkage [41]. Although there have been scarce reports of blueshifting of the

absorption edge with increasing temperature in Pb-based semiconductors [42], this behavior has not been reported for $CsPbBr_3$. However, in the case of CdMnTe crystals blueshifting of a $Mn^{2+}$ emission peak with temperature above 60 K has been observed. The ~ 0.04 eV shift was attributed to a multiphonon-assisted step-up process [43]. In this process, the carriers can reach a higher energy state due to phonon absorption which is enhanced with increasing temperature. The observed blueshift of emission peaks in $CsPbBr_3$ by ~0.04 eV (Fig. 4a) is consistent with such a multiphonon process.

In the case of $CsPbCl_3$ the blueshift of the emission peaks is also unexpected (Fig. 4b). The blueshift of the exciton luminescence spectra has been previously observed in the 4.2 - 77 K range [24] and attributed to the activation of a higher energy radiative exciton state above the conduction band edge. Furthermore a blueshift in the reflection spectra near the band edge was observed from 4.2 to 200 K indicating a widening of the bandgap as temperature increases, with transitions possibly tracking with the band edge [24]. Therefore, the blueshift with increasing T for $CsPbCl_3$ below 100 K is attributed to the temperature-dependent bandgap widening. Above 100 K, however, the peak energies become invariant with temperature or redshift, although all peaks remain above the bandgap (Fig. 4b). This behavior may be partly due to the phase transition of the crystal at ~185 K [44]. $CsPbCl_3$ undergoes another phase transition from monoclinic to triclinic between 194 and 185 K [9,20,45]

To determine the phonon energy, $E_{ph}$, the full-width half maximum (FWHM) $\omega(T)$ of the

band edge PL emission for both compounds were measured as a function of temperature. The temperature dependence of peak width for excitonic peaks was analyzed using Toyozawa's equation [46,47]

$$\omega(T) = \frac{A}{[\exp\left(\frac{E_{ph}}{k_B T}\right) - 1]} + C \quad (3)$$

where $\omega(T)$ is the peak FWHM and $C$ is a constant linewidth at low temperatures due to the absence of phonon broadening. From the analysis of spectral data shown in Fig. 5a using Eqn. (3), a phonon energy of 0.016 eV was calculated for $CsPbBr_3$. This value is in good agreement with the value of a single phonon energy of 0.016 eV [17] as well as 0.019 eV [4], previously obtained for this material using Raman spectroscopy, .

Fig. 5b shows the plot of ω(T) vs T for $CsPbCl_3$. The curve, however, is discontinuous at lower temperature and likely due to a reported phase transition at ~185 K [44]. The material is tetragonal based on our single-crystal refinement at room temperature and possibly over the whole 194- 310 K range due to distortion of the perovskite structure. As a result of this structural phase change the data has only been fitted for the values from 185 K to room temperature. A value of 0.043 eV is calculated for $E_{ph}$ using Eqn. (3). This value is in good agreement with a previously reported value of 0.046 eV for an LO phonon in $CsPbCl_3$ [48].

Thermal quenching of the PL can be analyzed using the two-step quenching model [49]

$$I(T) = \frac{I_0}{1 + C_1 \exp\left(-\frac{E_1}{k_B T}\right) + C_2 \exp(-\frac{E_2}{k_B T})} \quad (4)$$

where $I_0$ is the peak intensity at 0 K, $E_1$ and $E_2$ are the high and low-temperature activation

energies of non-radiative pathways, and $C_1$ and $C_2$ are related to the strength of the quenching processes. In the case of $CsPbBr_3$ the best fit analysis of the data in Fig. 6a to Eqn. (4) yields values of 0.017 eV and 0.0007 eV for $E_1$ and $E_2$, respectively. $E_1$ is often equated to the exciton binding energy [46,50] but in this case is about half as much as that previously reported for this compound [4,23]. Furthermore the agreement between the values obtained from Eq. 3 and Eq. 4 indicates that E1 is the phonon energy.

For $CsPbCl_3$, values of 0.057 eV and 0.0076 eV for $E_1$ and $E_2$, respectively, were obtained from the least squares analysis of the data in Fig. 6b to Eqn. (4). The value of $E_1$ is in excellent agreement with the value of 0.052 eV reported by Belikovich et al for the activation energy of radiationless transitions in $CsPbCl_3$ [25]. $CsPbX_3$ compounds have previously been reported to have large exciton binding energies, consistent with excitonic emissions persisting up to room temperature [4]. Their exciton binding energies are also consistent with those of semiconductors with similar bandgaps [51].

*Power dependent PL Studies*

The nature of recombination process can be identified from the dependence of the PL intensity on the excitation power [23]. It has been shown that the luminescence intensity $I$ of the near-band-edge photoluminescence (NBEPL) emission lines is proportional to $L^{\gamma}$, where $L$ is the power of the exciting laser radiation and $1 < \gamma < 2$ for exciton-like transition and $\gamma < 1$ for

free-to-bound and donor-acceptor pair (DAP) transitions[28]. All but one peak in the measured spectra have values of γ greater than 1 at low power (Figs. 7, 8). This indicates that the recombination involves excitons. The exception is the 2.98 eV peak in $CsPbCl_3$ with a γ-value of unity within error (γ = 0.94±0.15). The peak position, however, shows a blueshift as the excitation power is increased (Fig. 9b), which is not consistent with the behavior of a free to bound transition [52]. Therefore the power dependent PL measurements for $CsPbX_3$ indicate that all peaks are excitonic in nature.

The plot of integrated PL intensity vs laser power for $CsPbBr_3$ indicates that while the signals increase in intensity in the 0-10 mW range, a clear reduction in emission intensity is evident when the sample is irradiated with laser intensity higher than 10 mW (Fig. 7). This is unexpected since PL intensity should increase with increasing laser intensity. There are two possible mechanisms which can produce this effect. Due to our experimental conditions of high excitation power, this behavior could be attributed to carrier scattering effects. For a high concentration of photo-excited carriers, screening, scattering or self-annihilation of excitons occurs, decreasing the overall PL intensity at high excitation [53]. The other possibility is that PL fatigue is present in the material, characterized by a reduction in PL signal intensity as a function of time under prolonged light irradiation [51]. Since the scans for each laser intensity level are done with only a few minutes between scans, it is possible that the material does not have time to equilibrate before being excited again. This PL fatigue has also previously been

observed in chalcogenide glasses,[54] GaAs [55] and amorphous Si [56]. It should be noted, however, that PL fatigue has not been observed in $CsPbBr_3$ crystals and is currently under investigation to be presented elsewhere. The PL intensity reduction phenomenon was not observed in $CsPbCl_3$ in this study, possibly due to the lower excitation power that was used.

As to the identity of the defects, calculations of the defect formation energy in $CsPbBr_3$ using density functional theory (DFT) indicate a series of defect levels attributed to native defects. In this study, we considered vacancies ($V_{Cs}$, $V_{Pb}$, $V_{Br}$ ) and antisite defects ($Cs_{Pb}$, $Pb_{Cs}$, $Pb_{Br}$, $Br_{Pb,}$ $Cs_{Br}$, and $Br_{Cs}$). In Fig. 10(a), $\Delta H_D$ of $V_{Cs}$, $V_{Pb}$, $V_{Br}$, $Cs_{Pb}$, $Pb_{Cs}$, $Br_{Cs}$, and $Br_{Pb}$ are presented as a function of $E_F$ with three different growth conditions (Cs-poor only, Br-poor only, and a combination of Cs and Br deficiencies). The formation energies ($\Delta H_D$) of the antisite defects $Pb_{Br}$ and $Cs_{Br}$ are high and they are unlikely to be present. Calculations indicate that $V_{Cs}$, $V_{Pb}$ ,$Cs_{Pb}$ ,and $Br_{Cs}$ have shallow acceptor levels (≤ 0.1 eV) and $V_{Br}$ and $Pb_{Cs}$ donor levels with relatively low defect formation energy, in agreement with recent DFT defect studies on $CsPbBr_3$ and other halide perovskites [39,57]. In contrast, $Br_{Pb}$ has deep acceptor levels at 1.40 eV and 1.61 eV within the gap; however its $\Delta H_D$ is high which leads to a low concentration of this defect. Its maximum concentration under Cs-poor condition is $10^{13}$ $cm^{-3}$ at 650K.

The most dominant defects are then $V_{Cs}$, $V_{Pb}$, $Pb_{Cs}$ and $V_{Br}$. Of these, $V_{Cs}$, $V_{Pb}$, $Pb_{Cs}$ result in shallow levels within the bandgap, while $V_{Br}$ has states ~0.23 eV and ~0.24 eV above the bandgap. These values for $V_{Br}$ are in reasonable agreement with those recently obtained by Shi

and Du (0.16 eV, [39]) and supports the experimental PL peak positions in the current study. Fig. 10(b) summarizes calculated native defect levels of $CsPbBr_3$. The fact that no significant concentration of stable charged deep level defects are observed in $CsPbBr_3$ indicates potentially good charge transport properties in the form of high $\mu\tau$ values for efficient charge collection in detector devices.

## IV. Conclusion

Excitonic emissions in above gap luminescence in single crystal perovskite compounds $CsPbX_3$ (X = Cl, Br) were observed. Power and temperature dependent photoluminescent properties are presented from 10 K up to 290 K. The power dependent PL studies indicate that all peaks are excitonic in nature for both compounds. Both compounds exhibit above-bandgap luminescence which blueshifts with increasing temperature. $CsPbBr_3$ shows evidence of an above bandgap state located 0.16 eV above the conduction band minimum, corresponding to the peak energy seen in the PL. This energy level is attributed to a Br vacancy that has also been predicted in DFT calculations. In both $CsPbBr_3$ and $CsPbCl_3$ all emission peaks undergo a blueshift with increasing temperature. For $CsPbBr_3$, phonon-assisted processes are responsible for the blueshift, while in $CsPbCl_3$ the blueshift is attributed to a widening of the bandgap. No deep level or DAP luminescent peaks are observed in the PL spectrum of the $CsPbX_3$ perovskite compounds. These results indicate that the Bridgman grown materials may be suitable for hard radiation detector applications due to the absence of radiative deep level defects.

335

336 **ACKNOWLEDGEMENT**

337 This work is supported by the U.S. Department of Energy (NNSA) under Contract DE-AC02-
338 06CH11357. The theory part was supported by the Department of Homeland Security with
339 grant 2010-DN-077-ARI042-02 and. The authors thank Kyle McCall for technical assistance.

340

## Supplementary Material

The experimentally determined crystals structures of $CsPbBr_3$ (supercell) and $CsPbCl_3$ (subcell and supercell) as generated by the crystallographic .cif files are provided as Supporting information to this manuscript. The .cif files are also provided as Supplementary materials to this manuscript.

The $CsPbBr_3$ samples reported in this study were synthesized as follows: $PbBr_2$ is dissolved in 48% aqueous HBr and added slowly, under constant stirring at the initial steps, to a solution of CsBr dissolved in water. The mixture is left to cool down to ambient temperature and immediately filtered through a fritted-dish funnel under vacuum. The solid is washed with 8% aqueous HBr followed by methanol and dried overnight. The solid is further dried in an oven at ~ $70^0$C in air. The $CsPbCl_3$ samples were prepared similarly, with $Cs_2CO_3$ dissolved in 37% aqueous HCl being slowly added to PbO dissolved in 37% aqueous HCl under constant stirring to form the compound. The resulting $CsPbCl_3$ is filtered and dried as described above and then washed with 6% aqueous HCl followed by methanol and left for overnight drying. The solid is further dried in an oven at ~ $70^0$C in air.

Table 1. Crystal data and structure refinement for $CsPbCl_3$ at 293(2) K.

| Empirical formula | subcell | supercell |
|---|---|---|
| Formula weight | 446.45 | |
| Temperature | 293(2) K | |
| Wavelength | 0.71073 Å | |
| Crystal system | Tetragonal | Tetragonal |
| Space group | P4mm | I4/mmm |
| Unit cell dimensions | a = 5.5862(6) Å, α = 90°<br>b = 5.5862(6) Å, β = 90°<br>c = 5.5978(7) Å, γ = 90° | a = 11.1798(14) Å, α = 90°<br>b = 11.1798(14) Å, β = 90°<br>c = 11.1897(14) Å, γ = 90° |
| Volume | 174.68(4) $Å^3$ | 1398.6(4) $Å^3$ |
| Z | 1 | 8 |
| Density (calculated) | 4.244 $g/cm^3$ | 4.241 $g/cm^3$ |
| Absorption coefficient | 30.291 $mm^{-1}$ | 30.267 $mm^{-1}$ |
| F(000) | 188 | 1504 |
| Crystal size | 0.155 x 0.135 x 0.099 $mm^3$ | |
| Refinement method | Full-matrix least-squares on $F^2$ | |
| Completeness to θ | 100% | 100% |
| θ range for data collection | 3.640 to 28.978° | 2.575 to 29.094° |
| Index ranges | -7<=h<=7, -6<=k<=7, -7<=l<=7 | -15<=h<=15, -13<=k<=15, -15<=l<=15 |
| Reflections collected | 1678 | 6733 |
| Independent reflections | 317 [$R_{int}$ = 0.0679] | 586 [$R_{int}$ = 0.0859] |
| Data / restraints / parameters | 317 / 1 / 15 | 586 / 0 / 23 |
| Goodness-of-fit | 1.106 | 1.582 |
| Final R indices [I > 2σ(I)] | $R_{obs}$ = 0.0253, $wR_{obs}$ = 0.0627 | $R_{obs}$ = 0.0565, $wR_{obs}$ = 0.1976 |
| R indices [all data] | $R_{all}$ = 0.0253, $wR_{all}$ = 0.0627 | $R_{all}$ = 0.1272, $wR_{all}$ = 0.2414 |
| Extinction coefficient | .- | 0.0011(3) |
| Largest diff. peak and hole | 1.062 and -1.074 e·$Å^{-3}$ | 2.302 and -5.250 e·$Å^{-3}$ |

$R = \Sigma||F_o|-|F_c|| / \Sigma|F_o|$, $wR = \{\Sigma[w(|F_o|^2 - |F_c|^2)^2] / \Sigma[w(|F_o|^4)]\}^{1/2}$ and

$w=1/[\sigma^2(Fo^2)+(0.0393P)^2+0.1016P]$ where $P=(Fo^2+2Fc^2)/3$

Table 2. Crystal data and structure refinement for $CsPbBr_3$ supercell at 293(2) K.

| | |
|---|---|
| Empirical formula | $CsPbBr_3$ supercell |
| Formula weight | 579.83 |
| Temperature | 293(2) K |
| Wavelength | 0.71073 Å |
| Crystal system | Monoclinic |
| Space group | $P2_1/m$ |
| Unit cell dimensions | a = 11.6217(9) Å<br>α = 90°<br>b = 11.7398(9) Å<br>β = 90.325(6)°<br>c = 11.6257(9) Å<br>γ = 90° |
| Volume | 1586.1(2) $Å^3$ |
| Z | 8 |
| Density (calculated) | 4.856 $g/cm^3$ |
| Absorption coefficient | 40.793 $mm^{-1}$ |
| F(000) | 1936 |
| Crystal size | 0.027 x 0.020 x 0.007 $mm^3$ |
| θ range for data collection | 1.735 to 29.173° |
| Index ranges | -15<=h<=15<br>-16<=k<=15<br>-15<=l<=15 |
| Reflections collected | 15463 |
| Independent reflections | 4460 [$R_{int}$ = 0.0848] |
| Completeness to θ = 25.242° | 100% |
| Refinement method | Full-matrix least-squares on $F^2$ |
| Data / restraints / parameters | 4460 / 0 / 111 |
| Goodness-of-fit | 1.036 |
| Final R indices [I > 2σ(I)] | $R_{obs}$ = 0.0598, $wR_{obs}$ = 0.1306 |
| R indices [all data] | $R_{all}$ = 0.1197, $wR_{all}$ = 0.1602 |
| Extinction coefficient | 0.00305(15) |
| Largest diff. peak and hole | 2.394 and -2.924 e·$Å^{-3}$ |

$R = \Sigma||F_o|-|F_c|| / \Sigma|F_o|$, $wR = \{\Sigma[w(|F_o|^2 - |F_c|^2)^2] / \Sigma[w(|F_o|^4)]\}^{1/2}$ and $w=1/[\sigma^2(Fo^2)+(0.0617P)^2]$ where $P=(Fo^2+2Fc^2)/$

Table 3. Atomic coordinates (x$10^4$) and equivalent isotropic displacement parameters (Å$^2$x$10^3$) for $CsPbCl_3$ at 293(2) K with estimated standard deviations in parentheses.

| Label | x | y | z | Occupancy | $U_{eq}$* |
|---|---|---|---|---|---|
| | | | $CsPbCl_3$ supercell (*P*4*mm*) | | |
| Pb(1) | 0 | 0 | -1(1) | 1 | 28(1) |
| Cs(1) | 5000 | 5000 | 4930(40) | 1 | 80(1) |
| Cl(1) | 5000 | 0 | 480(40) | 1 | 134(7) |
| Cl(2) | 0 | 0 | 5100(120) | 1 | 138(7) |
| | | | $CsPbCl_3$ supercell (*I*4/*mmm*) | | |
| Pb(1) | 2500 | 2500 | 2500 | 1 | 37(1) |
| Cs(1) | 5000 | 0 | 0 | 1 | 76(2) |
| Cs(2) | 0 | 0 | 0 | 1 | 117(4) |
| Cs(3) | 5000 | 5000 | 0 | 1 | 112(4) |
| Cl(1) | 2260(20) | 2260(20) | 0 | 1 | 180(16) |
| Cl(2) | 2547(14) | 0 | 2679(16) | 1 | 132(8) |

*$U_{eq}$ is defined as one third of the trace of the orthogonalized$U_{ij}$ tensor.

Table 4. Atomic coordinates (x$10^4$) and equivalent isotropic displacement parameters (Å$^2$x$10^3$) for $CsPbBr_3$ at 293(2) K with estimated standard deviations in parentheses.

| Label | x | y | z | Occupancy | $U_{eq}$* |
|---|---|---|---|---|---|
| | | | | | |
| | | $CsPbBr_3$ supercell (*Pnma*) | | | |
| Pb | 0 | 5000 | 0 | 1 | 20(1) |
| Cs | 5310 (3) | 2500 | 70(2) | 1 | 75(1) |
| Br(1) | 2935(2) | 4761(2) | 2061(2) | 1 | 59(1) |
| Br(2) | 37(3) | 7500 | 455(4) | 1 | 72(1) |
| | | $CsPbBr_3$ supercell ($P2_1/m$) | | | |
| Pb(1) | 0 | 0 | 0 | 1 | 25(1) |
| Pb(2) | 5000 | 0 | 5000 | 1 | 27(1) |
| Pb(3) | 5000 | 0 | 0 | 1 | 31(1) |
| Pb(4) | 0 | 0 | 5000 | 1 | 19(1) |
| Cs(1) | 7361(4) | 2500 | 2680(6) | 1 | 81(2) |
| Cs(2) | 2368(4) | 2500 | 7609(6) | 1 | 90(2) |
| Cs(3) | 2312(5) | 2500 | 2592(4) | 1 | 77(2) |
| Cs(4) | 7264(5) | 2500 | 7589(4) | 1 | 74(2) |
| Br(1) | 2498(3) | 166(4) | 371(4) | 1 | 74(2) |
| Br(2) | 2497(3) | -194(4) | 4634(4) | 1 | 72(2) |
| Br(3) | 9520(3) | 271(4) | 2496(3) | 1 | 56(1) |
| Br(4) | 4523(3) | 265(4) | 7498(2) | 1 | 56(1) |
| Br(5) | 5216(8) | 2500 | 229(7) | 1 | 84(3) |
| Br(6) | 210(7) | 2500 | 5239(7) | 1 | 76(2) |
| Br(7) | 4771(6) | 2500 | 4750(6) | 1 | 67(2) |
| Br(8) | 9913(8) | 2500 | -272(7) | 1 | 96(3) |

*$U_{eq}$ is defined as one third of the trace of the orthogonalized$U_{ij}$ tensor.

**List of Figure Captions**

Fig. 1. Ball-and-Stick representation of the unit cells of $CsPbCl_3$ and $CsPbBr_3$ for the corresponding subcell and supercells. Note that both structural refinements have been obtained by the same single-crystal by omitting or using the superlattice reflections observed using an image plate detector. Photographs of the corresponding crystal boule for $CsPbCl_3$ and $CsPbBr_3$, as obtained from the Bridgman-growth, are shown on each side of the crystal structure representation.

Fig. 2: (a) PL spectra of $CsPbBr_3$ from 10 K to 180 K. (inset) Two peaks are observed at 10 K, at 2.29 and 2.33 eV. A photograph of the green PL emission is also shown in the inset. (b) Spectra of $CsPbCl_3$ from 11 K to 290 K. (inset) at 11K (shown) and up to 100 K, 4 peaks are seen: 2.94, 2.96, 2.97, and 2.98 eV. Above 100 K, and up to 290 K all peaks except that at 2.94 eV are seen. A photograph of the blue PL emission is also shown in the inset.

Fig. 3: Plots of $\alpha^2$ vs energy of (a) $CsPbBr_3$ and (b) $CsPbCl_3$ single crystals, calculated from transmission measurements at room temperature.

Fig. 4: (a) Peak position vs temperature, $CsPbBr_3$. The excitation intensity is 31.6 mW. The peak positions for both peaks are observed to blue-shift with increasing temperature. (b) Peak position vs. T, $CsPbCl_3$. The excitation intensity is 15.8 mW. The peak position is expected to continuously red-shift as T increases, but this is only observed above ~150 K, and is not seen for the peak at 2.98 eV. This blue shift seen in both compounds may result from carrier screening due to a large concentration of carriers generated by the high excitation intensity and thermal generation.

Fig. 5: (a) Peak FWHM vs T for $CsPbBr_3$. Fitting the data with Eqn. (1) yields values of 0.016 eV $E_{ph.}$ (b) Peak FWHM vs T, $CsPbCl_3$. Only the region from 190-300K can be fitted with Eqn. (1) since the material undergoes a phase transition at 185 K. The analysis yields values of 0.043 eV for $E_{ph.}$

Fig. 6: (a) Peak intensity vs 1/T, $CsPbBr_3$. Analysis of this data with Eqn. (2) indicates that the high and low temperature activation energies are is 0.017 and 0.0007 eV. (b) Peak intensity vs 1/T, $CsPbCl_3$. Analysis of this data indicates that the high and low temperature activation energies are is 0.057 and 0.0076 eV.

Fig. 7: Log PL intensity vs log incident laser intensity, $CsPbBr_3$. The laser intensity was varied from 2 to 91 mW. A linear fit of the low excitation region (solid line) shows slopes of 1.1 and

1.4 for both peaks, indicating excitonic nature. The PL intensity decreases, however, above an incident laser power of 10 mW for the shoulder peak, and 31.6 mW for the main peak.

Fig. 8: log PL intensity vs log laser power for the 3 peaks seen at higher temperatures in $CsPbCl_3$. The laser intensity was varied from 2 to 50 mW. Linear fits are shown by the solid black lines. The γ values are 1.75 for (a), 1.57 for (b), and 0.94 for (c). These correspond to the peaks at 2.96, 2.97, and 2.98 eV respectively.

Fig. 9: (a) Peak position vs. incident laser power for $CsPbBr_3$ at 10 K. (b) Peak position vs. laser power, $CsPbCl_3$ at 10K.

Fig. 10: (a) Calculated defect formation energy in the $CsPbBr_3$ are plotted as a function of Fermi level. Left and right panels correspond to Cs-poor and Br-poor conditions, respectively. The middle panel is plotted for the mid-condition between Cs-poor and Br-poor. Equilibrium Fermi level $E_F^{eq}$ is plotted as black vertical dotted-line. (b) Defect levels for vacancy and antisite defect of $CsPbBr_3$ are summarized. Defect levels are presented with respect to the valence band maximum. Blue and red at the bottom of figure means acceptor and donor type, respectively.

450 Figures

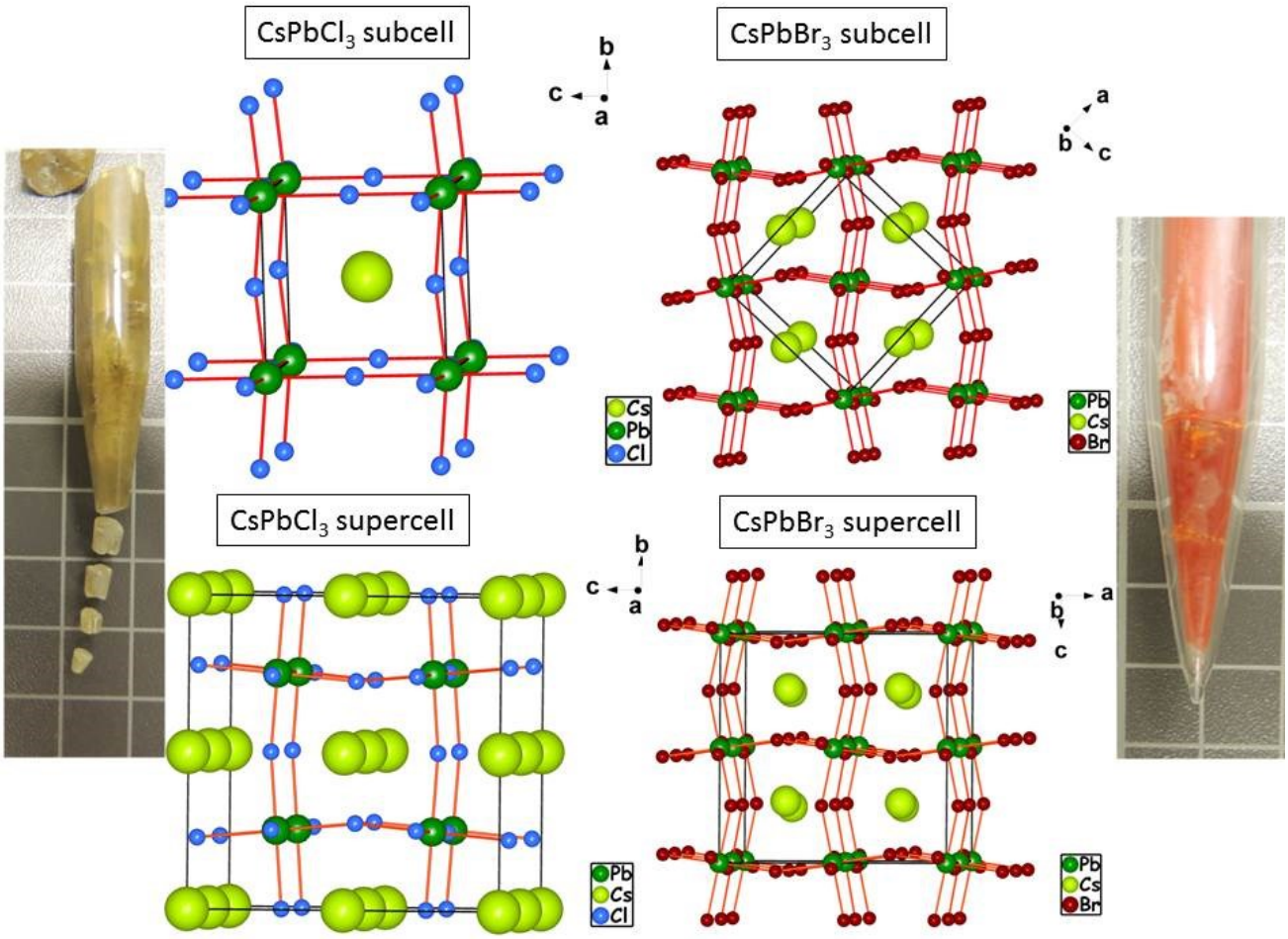


Fig. 1

451

452

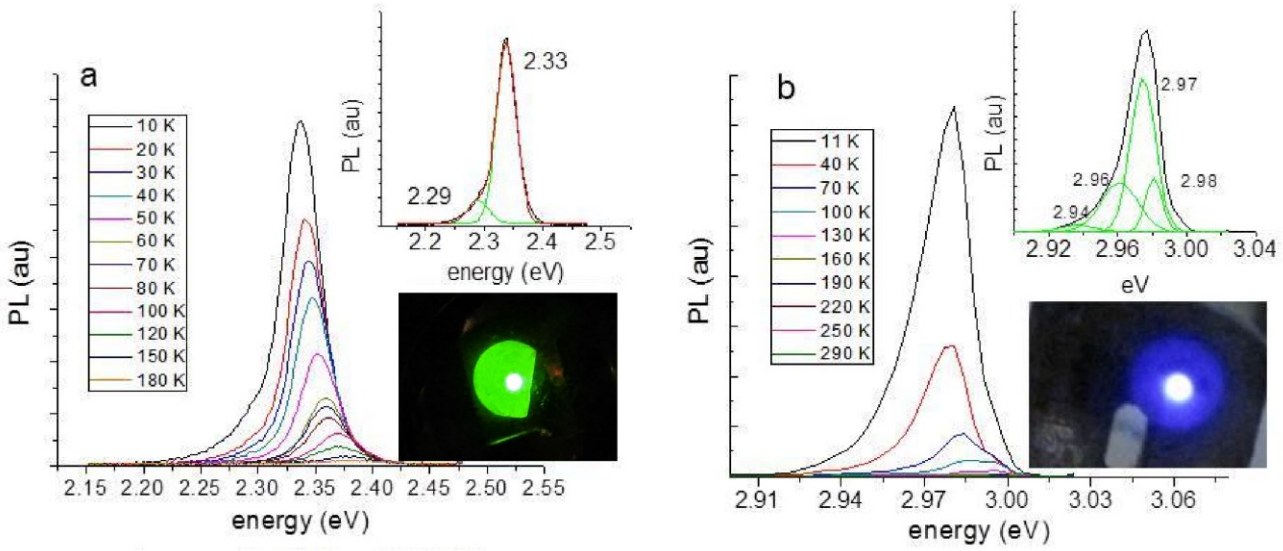
a
10 K
20 K
30 K
40 K
50 K
60 K
70 K
80 K
100 K
120 K
150 K
180 K
PL (au)
2.15 2.20 2.25 2.30 2.35 2.40 2.45 2.50 2.55
energy (eV)
PL (au)
2.33
2.29
2.2 2.3 2.4 2.5
energy (eV)
b
11 K
40 K
70 K
100 K
130 K
160 K
190 K
220 K
250 K
290 K
PL (au)
2.91 2.94 2.97 3.00 3.03 3.06
energy (eV)
PL (au)
2.97
2.96
2.98
2.94
2.92 2.96 3.00 3.04
eV

Fig. 2.

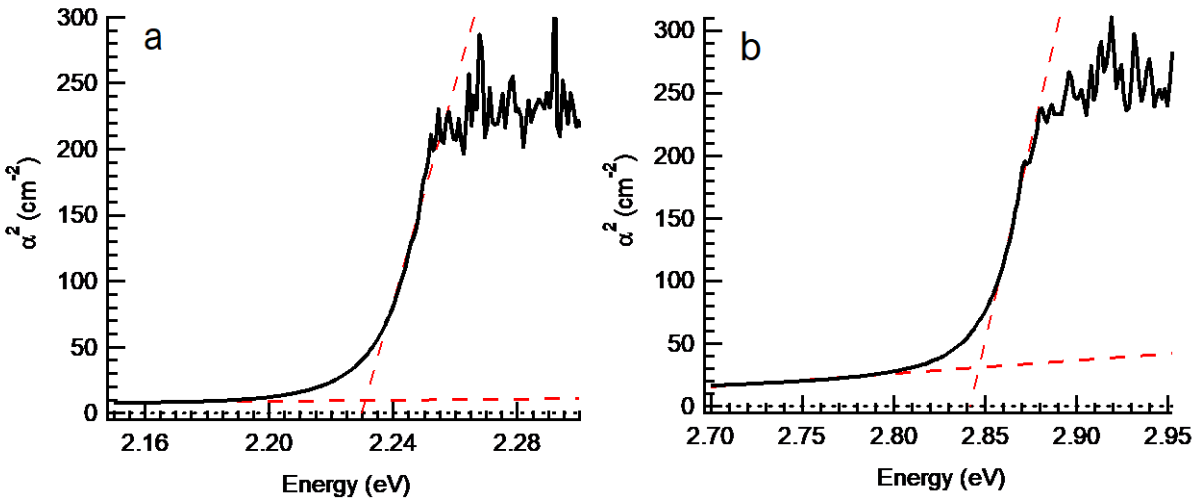
a
b
$\alpha^2$ (cm$^{-2}$)
Energy (eV)
300
250
200
150
100
50
0
2.16
2.20
2.24
2.28
2.70
2.75
2.80
2.85
2.90
2.95

Fig. 3.

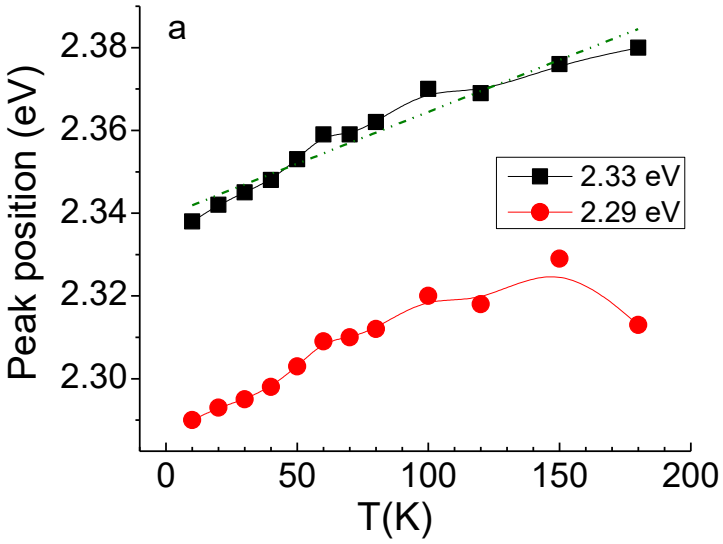


460

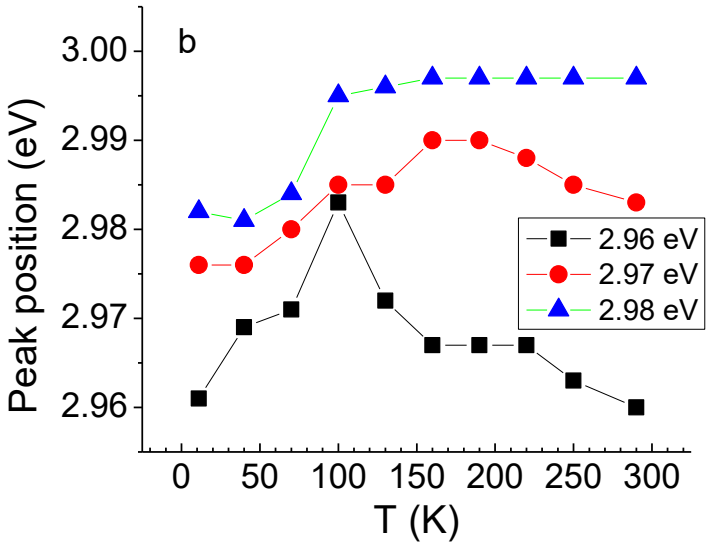


461

462 Fig. 4

463

464

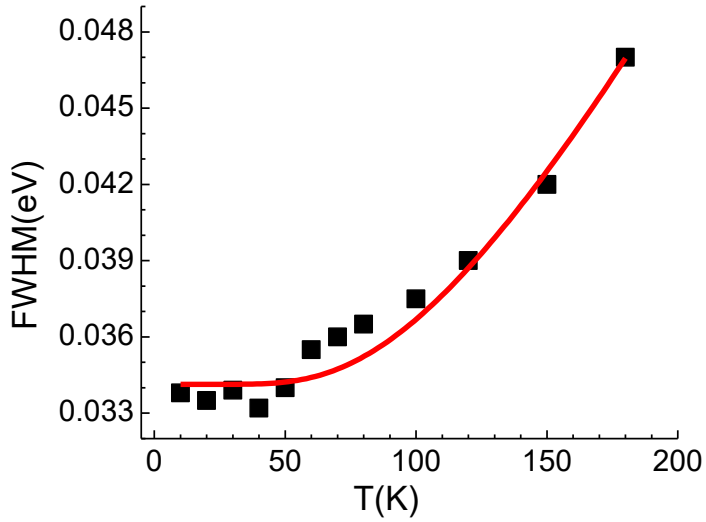
0.048
0.045
0.042
0.039
0.036
0.033
FWHM(eV)
0
50
100
150
200
T(K)

(b)

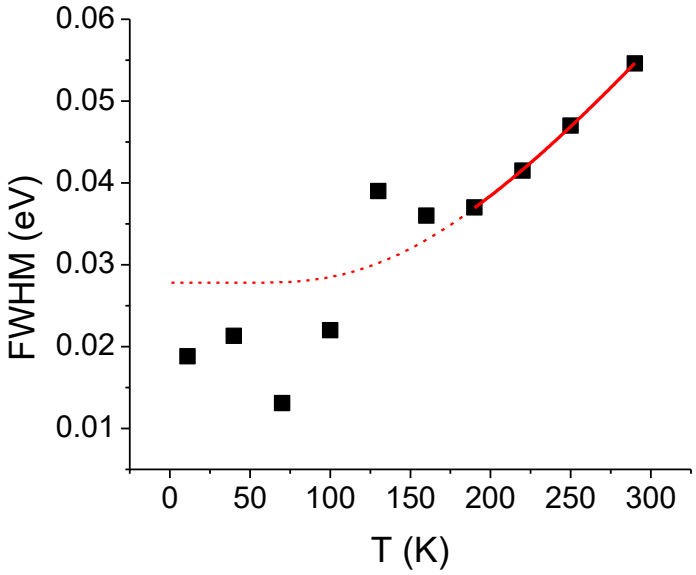
0.06
0.05
0.04
0.03
0.02
0.01
FWHM (eV)
0
50
100
150
200
250
300
T (K)

Fig. 5

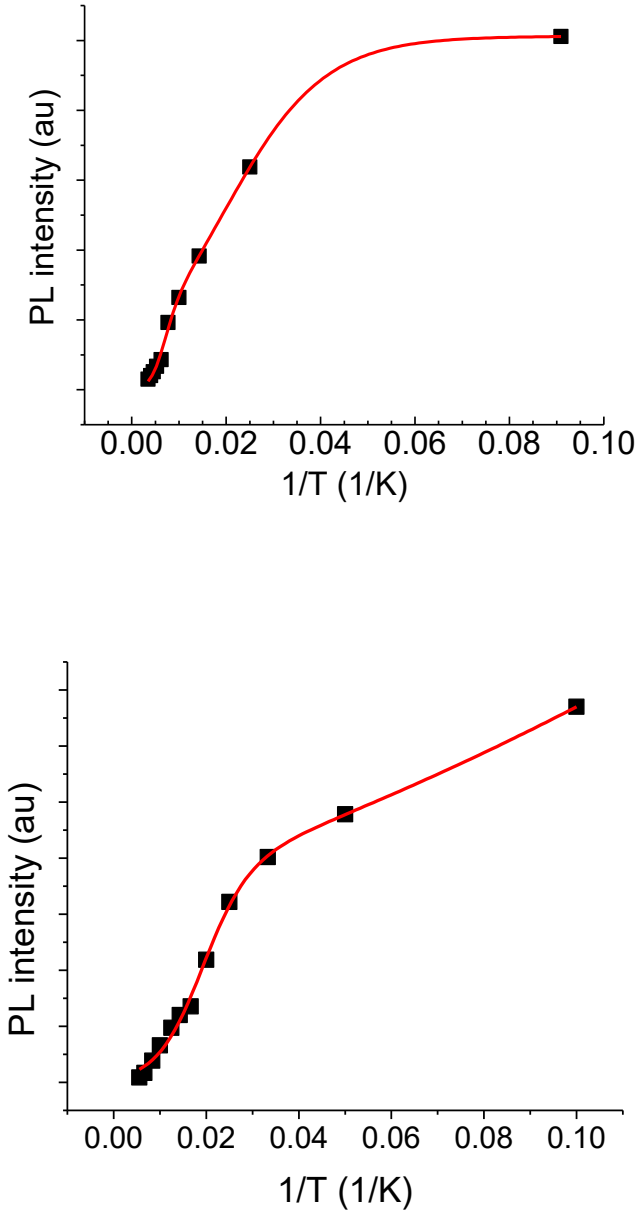
PL intensity (au)
0.00
0.02
0.04
0.06
0.08
0.10
1/T (1/K)
PL intensity (au)
0.00
0.02
0.04
0.06
0.08
0.10
1/T (1/K)

Fig. 6

465

466

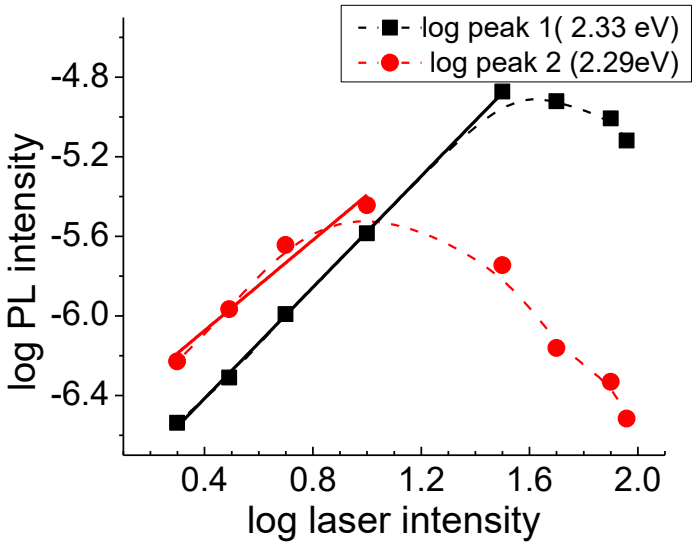
log peak 1( 2.33 eV)
log peak 2 (2.29eV)
log PL intensity
-4.8
-5.2
-5.6
-6.0
-6.4
0.4
0.8
1.2
1.6
2.0
log laser intensity

Fig. 7

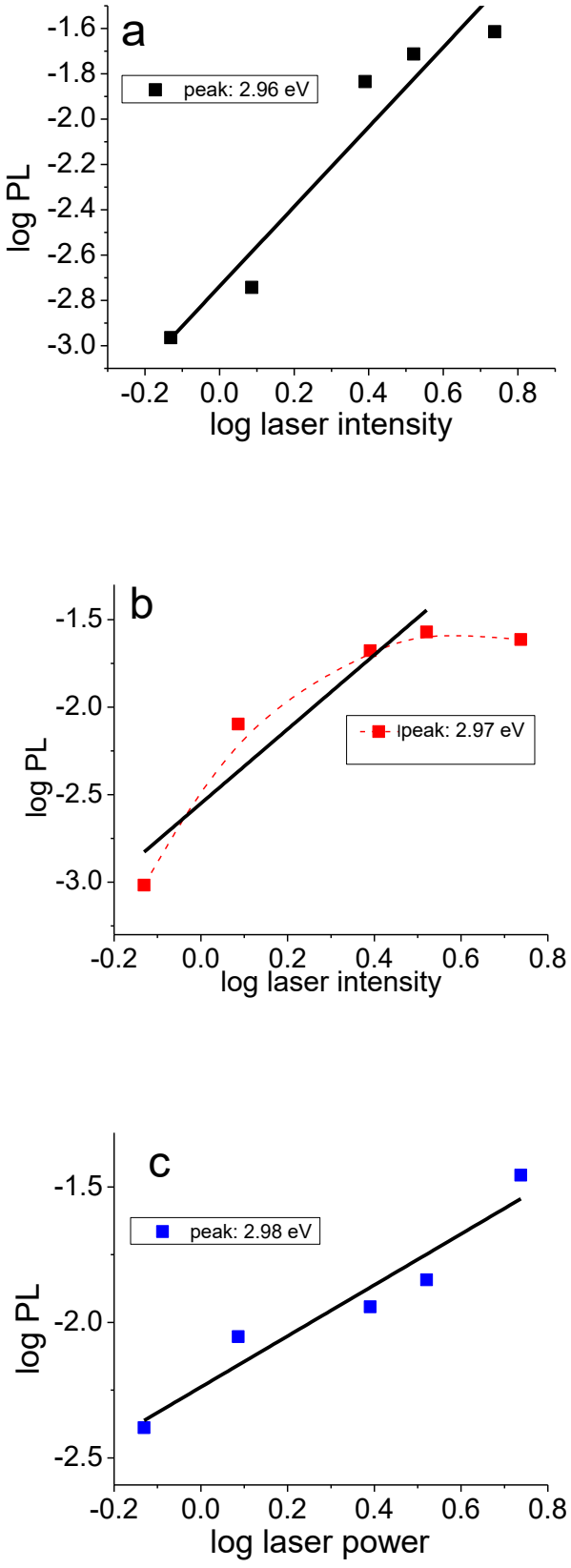
a
peak: 2.96 eV
log PL
log laser intensity
b
Ipeak: 2.97 eV
log PL
log laser intensity
c
peak: 2.98 eV
log PL
log laser power

Fig. 8

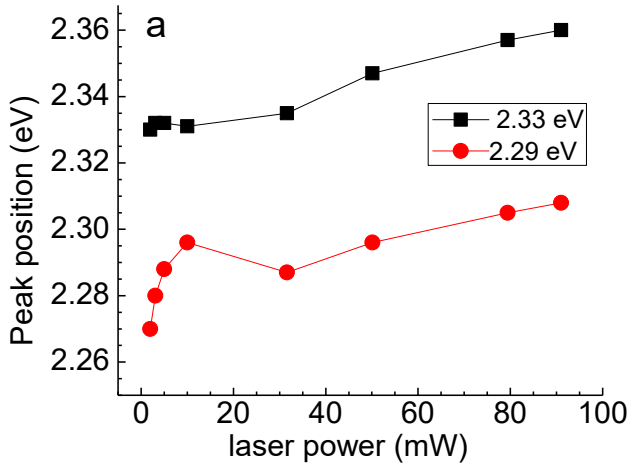
a
2.36
2.34
2.32
2.30
2.28
2.26
Peak position (eV)
0
20
40
60
80
100
laser power (mW)
2.33 eV
2.29 eV

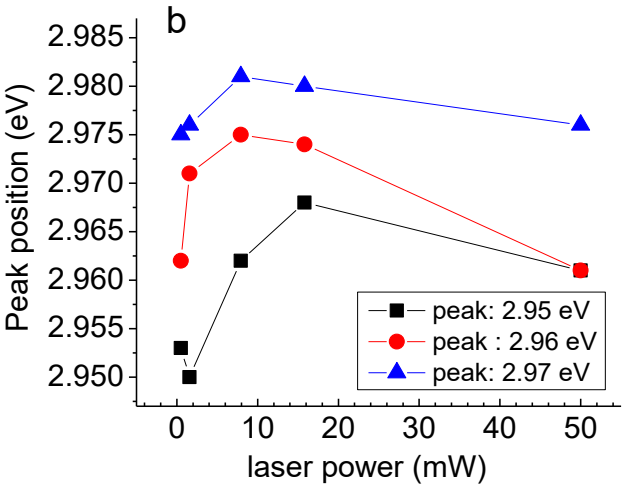
b
2.985
2.980
2.975
2.970
2.965
2.960
2.955
2.950
Peak position (eV)
0
10
20
30
40
50
laser power (mW)
peak: 2.95 eV
peak : 2.96 eV
peak: 2.97 eV

Fig. 9.

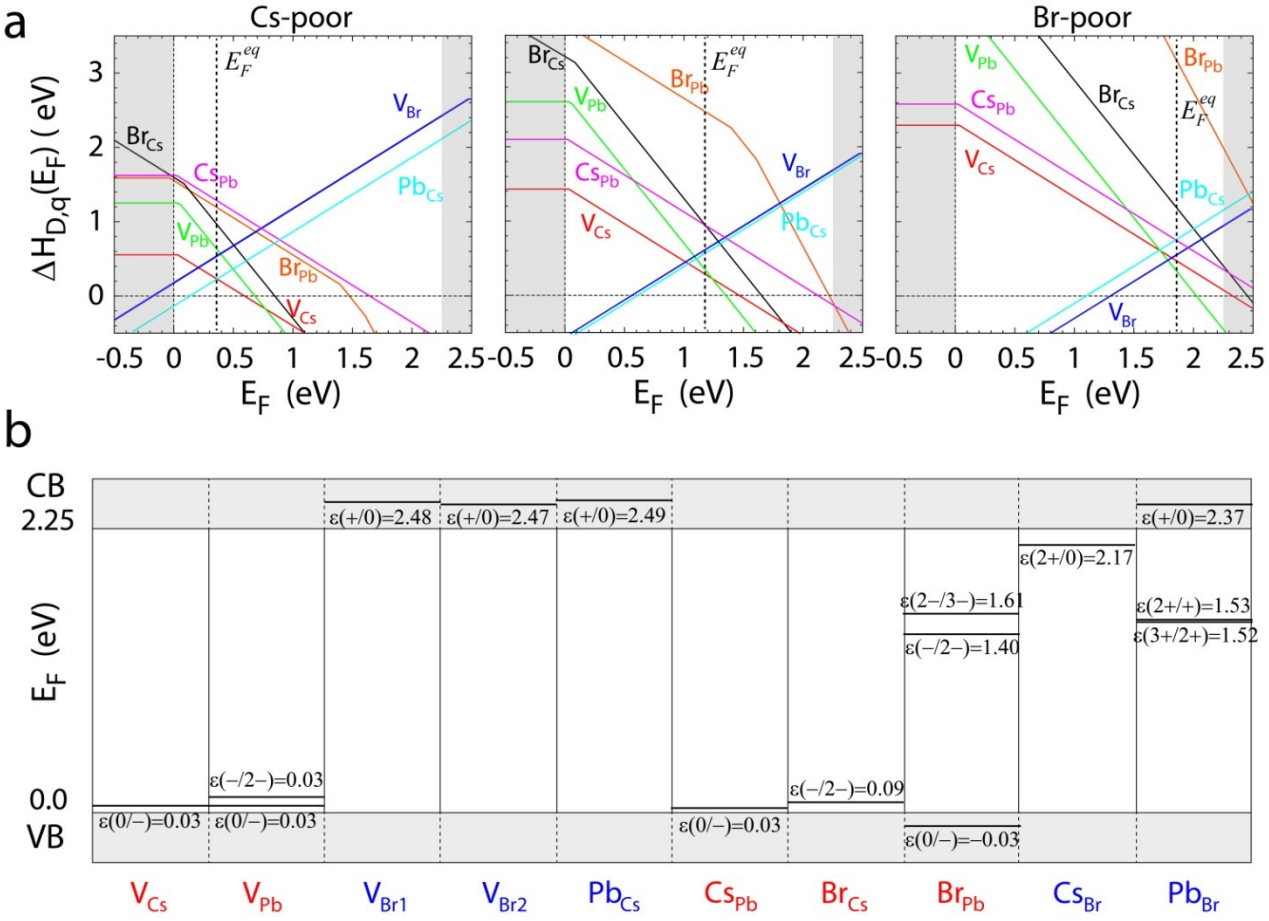
a
Cs-poor
Br-poor
$\Delta H_{D,q}(E_F)$ ( eV)
$E_F$ (eV)
$E_F^{eq}$
$Br_{Cs}$
$Cs_{Pb}$
$V_{Br}$
$Pb_{Cs}$
$V_{Pb}$
$Br_{Pb}$
$V_{Cs}$
b
CB
2.25
$E_F$ (eV)
0.0
VB
ε(+/0)=2.48
ε(+/0)=2.47
ε(+/0)=2.49
ε(+/0)=2.37
ε(2+/0)=2.17
ε(2−/3−)=1.61
ε(2+/+)=1.53
ε(−/2−)=1.40
ε(3+/2+)=1.52
ε(−/2−)=0.03
ε(−/2−)=0.09
ε(0/−)=0.03
ε(0/−)=0.03
ε(0/−)=0.03
ε(0/−)=−0.03
$V_{Cs}$
$V_{Pb}$
$V_{Br1}$
$V_{Br2}$
$Pb_{Cs}$
$Cs_{Pb}$
$Br_{Cs}$
$Br_{Pb}$
$Cs_{Br}$
$Pb_{Br}$

Fig. 10.

## References


1 C. K. Moller, *Nature* **182** (4647), 1436 (1958).

2 C. K. Moller, *Mat. Fys. Medd. Dan. Vid. Selsk* **32** (2), 1-27 (1959).

3 C. K. Moller, *Mat. Fys. Medd. Dan. Vid. Selsk* **32** (1), 1-18 (1959).

4 I. P. Pashuk, N. S. Pidzyrailo, and M. G. Matsko, *Sov. Phys. Solid State* **23** (7), 1263 (1981).

5 S. J. Clark, J. D. Donaldson, and J. A. Harvey, *J. Mater. Chem.* **5** (11), 1813-1818 (1995); M. Nikl, K. Nitsch, E. Mihóková, K. Polák, P. Fabeni, G. P. Pazzi, M. Gurioli, S. Santucci, R. Phani, A. Scacco, and F. Somma, *Physica E* **4** (4), 323-331 (1999); F. Somma, M. Nikl, K. Nitsch, P. Fabeni, and G. P. Pazzi, *J. Lumin.* **94–95** (0), 169-172 (2001); T. Sakuma, M. Mutou, K. Ohki, M. Arai, H. Takahashi, and Y. Ishii, *Solid State Ionics* **154–155**, 237-242 (2002); S.-i. Kondo, M. Kakuchi, A. Masaki, and T. Saito, *J. Phys. Soc. Jpn.* **72** (7), 1789-1791 (2003); S. Kondo, K. Suzuki, T. Saito, H. Asada, and H. Nakagawa, *Phys. Rev. B* **70** (20), 205322 (2004); S. Kondo, K. Takahashi, T. Nakanish, T. Saito, H. Asada, and H. Nakagawa, *Current Applied Physics* **7** (1), 1-5 (2007).

6 K. Nitsch, V. Hamplová, M. Nikl, K. Polák, and M. Rodová, *Chem. Phys. Lett.* **258** (3-4), 518-522 (1996).

7 Y. H. Chang, C. H. Park, and K. Matsuishi, *J. Kor. Phys. Soc.* **44** (4), 889-893 (2004); G. Murtaza and I. Ahmad, *Physica B* **406** (17), 3222-3229 (2011).

8 M. Natarajan and B. Prakash, *Phys. Status Solidi A* **4** (3), K167-K172 (1971); S. Hirotsu, J. Harada, M. Iizumi, and K. Gesi, *J. Phys. Soc. Jpn.* **37** (5), 1393-1398 (1974).

9 M. I. Cohen, K. F. Young, T. T. Chang, and W. S. Brower, *J. Appl. Phys.* **42** (13), 5267-5272 (1971).

10 J. Hutton, R. J. Nelmes, G. M. Meyer, and V. R. Eiriksson, *J. Phys. C: Solid State Phys.* **12** (24), 5393 (1979); M. Sakata, T. Nishiwaki, and J. Harada, *J. Phys. Soc. Jpn.* **47** (1), 232-233 (1979); M. Sakata, J. Harada, M. J. Cooper, and K. D. Rouse, *Acta Crystallogr. Sect. A* **36** (1), 7-15 (1980).

11 A. Kojima, K. Teshima, Y. Shirai, and T. Miyasaka, *J. Am. Chem. Soc.* **131** (17), 6050-6051 (2009).

12 I. Chung, B. Lee, J. He, R. P. H. Chang, and M. G. Kanatzidis, *Nature* **485** (7399), 486-489 (2012).

13 L. Etgar, P. Gao, Z. Xue, Q. Peng, A. K. Chandiran, B. Liu, M. K. Nazeeruddin, and M. Grätzel, *J. Am. Chem. Soc.* **134** (42), 17396-17399 (2012); H.-S. Kim, C.-R. Lee, J.-H. Im, K.-B. Lee, T. Moehl, A. Marchioro, S.-J. Moon, R. Humphry-Baker, J.-H. Yum, J. E. Moser, M. Gratzel, and N.-G. Park, *Sci. Rep.* **2**, 591 (2012); M. M. Lee, J. Teuscher, T. Miyasaka, T. N. Murakami, and H. J. Snaith, *Science* **338** (6107), 643-647 (2012).

14 H. Zhou, Q. Chen, G. Li, S. Luo, T.-b. Song, H.-S. Duan, Z. Hong, J. You, Y. Liu, and Y. Yang, *Science* **345** (6196), 542-546 (2014).

15 O. Busmundrud and J. Feder, *Solid State Commun.* **9** (18), 1575-1577 (1971); J. Mizusaki,

K. Arai, and K. Fueki, *Solid State Ionics* **11** (3), 203-211 (1983); R. L. Narayan, M. V. S. Sarma, and S. V. Suryanarayana, *J. Mater. Sci. Lett.* **6** (1), 93-94 (1987).

16 Z. Liu, J. A. Peters, C. C. Stoumpos, M. Sebastian, B. W. Wessels, J. Im, A. J. Freeman, and M. G. Kanatzidis, presented at the Proc. SPIE, 2013 (unpublished).

17 C. C. Stoumpos, C. D. Malliakas, J. A. Peters, Z. Liu, M. Sebastian, J. Im, T. C. Chasapis, A. C. Wibowo, D. Y. Chung, A. J. Freeman, B. W. Wessels, and M. G. Kanatzidis, *Cryst. Growth Des.* **13** (7), 2722-2727 (2013).

18 S. Wang, Z. Liu, J. A. Peters, M. Sebastian, S. L. Nguyen, C. D. Malliakas, C. C. Stoumpos, J. Im, A. J. Freeman, B. W. Wessels, and M. G. Kanatzidis, *Cryst. Growth Des.* **14** (5), 2401-2410 (2014).

19 A. Owens, *Compound Semiconductor Radiation Detectors*. (Taylor & Francis, 2012).

20 K. Hitomi, Y. Kikuchi, T. Shoji, and K. Ishii, *IEEE Trans. Nucl. Sci.* **56** (4), 1859-1862 (2009).

21 M. Rodová, J. Brožek, K. Knížek, and K. Nitsch, *J. Therm. Anal. Calorim.* **71** (2), 667-673 (2003).

22 K. S. Aleksandrov, *Ferroelectrics* **14** (1), 801-805 (1976); C. J. Howard and H. T. Stokes, *Acta Crystallogr. Sect. A* **61** (1), 93-111 (2005).

23 D. Fröhlich, K. Heidrich, H. Künzel, G. Trendel, and J. Treusch, *J. Lumin.* **18-19, Part 1**, 385-388 (1979).

24 L. N. Amitin, A. T. Anistratov, and A. I. Kuznetsov, *Fiz. Tverd. Tela (Leningrad)* **21** (12), 3535-3541 (1979).

25 B. A. Belikovich, I. P. Pashchuk, and N. S. Pidzyrailo, *Opt. Spectrosc.* **42**, 62-64 (1977).

26 K. Goksen, N. M. Gasanly, and R. Turan, *Cryst. Res. Technol.* **41** (8), 822-828 (2006).

27 J. Krustok, H. Collan, and K. Hjelt, *J. Appl. Phys.* **81** (3), 1442-1445 (1997).

28 T. Schmidt, K. Lischka, and W. Zulehner, *Phys. Rev. B* **45** (16), 8989-8994 (1992); A. Bauknecht, S. Siebentritt, J. Albert, and M. C. Lux-Steiner, *J. Appl. Phys.* **89** (8), 4391-4400 (2001).

29 G. M. Sheldrick, *Acta Crystallogr. Sect. A* **64** (1), 112-122 (2008).

30 A. L. Spek, *Acta Crystallographica Section D* **65** (2), 148-155 (2009).

31 L. Farrugia, *J. Appl. Crystallogr.* **45** (4), 849-854 (2012).

32 P. E. Blöchl, *Phys. Rev. B* **50** (24), 17953-17979 (1994).

33 G. Kresse and J. Hafner, *Phys. Rev. B* **47** (1), 558-561 (1993); G. Kresse and J. Furthmüller, *Phys. Rev. B* **54** (16), 11169-11186 (1996).

34 J. P. Perdew, K. Burke, and M. Ernzerhof, *Phys. Rev. Lett.* **77** (18), 3865-3868 (1996).

35 J. Heyd, G. E. Scuseria, and M. Ernzerhof, *The Journal of Chemical Physics* **118** (18), 8207-8215 (2003); J. Heyd, G. E. Scuseria, and M. Ernzerhof, *The Journal of Chemical Physics* **124** (21), 219906 (2006).

36 C. Freysoldt, B. Grabowski, T. Hickel, J. Neugebauer, G. Kresse, A. Janotti, and C. G. Van de Walle, *Reviews of Modern Physics* **86** (1), 253-305 (2014).

37 S. Lany and A. Zunger, *Phys. Rev. B* **78** (23), 235104 (2008).

38 D. Åberg, P. Erhart, A. J. Williamson, and V. Lordi, *Phys. Rev. B* **77** (16), 165206 (2008).

39 H. Shi and M.-H. Du, *Phys. Rev. B* **90** (17), 174103 (2014).

40 Q. Dong, Y. Fang, Y. Shao, P. Mulligan, J. Qiu, L. Cao, and J. Huang, *Science* **347** (6225), 967-970 (2015).

41 P. Lautenschlager, P. B. Allen, and M. Cardona, *Phys. Rev. B* **31** (4), 2163-2171 (1985).

42 V. D'Innocenzo, G. Grancini, M. J. Alcocer, A. R. S. Kandada, S. D. Stranks, M. M. Lee, G. Lanzani, H. J. Snaith, and A. Petrozza, *Nature communications* **5** (2014); N. Ashcroft, *Saunders College, Philadelphia* (1976).

43 H. Younghun, U. Youngho, and P. Hyoyeol, *J. Kor. Phys. Soc.* **58** (51), 1312 (2011).

44 K. Wu, A. Bera, C. Ma, Y. Du, Y. Yang, L. Li, and T. Wu, *Phys. Chem. Chem. Phys.* **16** (41), 22476-22481 (2014).

45 J. A. Cape, R. L. White, and R. S. Feigelson, *J. Appl. Phys.* **40** (13), 5001-5005 (1969).

46 C. J. Youn, T. S. Jeong, M. S. Han, and J. H. Kim, *J. Cryst. Growth* **261** (4), 526-532 (2004).

47 Y. Toyozawa, *Prog. Theor. Phys.* **27** (1), 89-104 (1962).

48 D. M. Calistru, L. Mihut, S. Lefrant, and I. Baltog, *J. Appl. Phys.* **82** (11), 5391-5395 (1997).

49 D. Bimberg, M. Sondergeld, and E. Grobe, *Phys. Rev. B* **4** (10), 3451-3455 (1971).

50 E. Cohen, R. A. Street, and A. Muranevich, *Phys. Rev. B* **28** (12), 7115-7124 (1983).

51 I. Pelant and J. Valenta, *Luminescence Spectroscopy of Semiconductors*. (Oxford University Press, New York, 2012).

52 S. Levcenko, V. E. Tezlevan, E. Arushanov, S. Schorr, and T. Unold, *Phys. Rev. B* **86** (4), 045206 (2012).

53 D. C. Reynolds, D. C. Look, and B. Jogai, *J. Appl. Phys.* **88** (10), 5760-5763 (2000); T.-R. Park, *J. Kor. Phys. Soc.* **44** (4), 930-933 (2004).

54 T. Nakanishi, Y. Tomii, and K. Hachiya, *Electrochim. Acta* **100**, 304-310 (2013); T. Nakanishi, Y. Tomii, and K. Hachiya, *J. Non-Cryst. Solids* **354** (15-16), 1627-1632 (2008); M. Seki and K. Hachiya, *J. Phys.: Condens. Matter* **15** (26), 4555 (2003).

55 D. Redfield and R. H. Bube, *Photoinduced Defects in Semiconductors*. (Cambridge University Press, 1996).

56 I. Hirabayashi, K. Morigaki, and S. Nitta, *Japanese Journal of Applied Physics* **19** (7), L357 (1980); D. Redfield and R. H. Bube, *Appl. Phys. Lett.* **54** (11), 1037-1039 (1989).

57 W.-J. Yin, T. Shi, and Y. Yan, *Appl. Phys. Lett.* **104** (6), 063903 (2014).